RSC Advances

PAPER

View Article Online
View Journal | View Issue

Cite this: *RSC Adv.*, 2022, **12**, 6352

Synthesis, spectroscopic findings and crystal engineering of Pb(II)–Salen coordination polymers, and supramolecular architectures engineered by σ-hole/spodium/tetrel bonds: a combined experimental and theoretical investigation†

Dhrubajyoti Majumdar, *[ab] A. Frontera, [c] Rosa M. Gomila, [c] Sourav Das [d] and Kalipada Bankura [a]

Spontaneous self-assembly is one of the available synthetic routes to achieve structurally versatile and unique crystal complexes with selected metal–ligand combinations in the spirit of pseudohalides. In this endeavour, we designed a novel 1D coordination polymer (CP), $[(Cd)(Pb)(L)(\eta^1\text{-NCS})(\eta^1\text{-SCN})]_n$ (**1**), using a compartmental Salen ligand (H_3L) in the presence of NaSCN. The characterization of the CP was accomplished using several spectroscopic techniques: MALDI-TOF, PXRD, SEM, EDX mapping, and single-crystal X-ray crystallography. The CP crystallizes in the monoclinic space group $P2_1/c$ with $Z = 4$. SCXRD reveals Cd(II) and Pb(II) metal ions fulfilled distorted square pyramidal and hemi-directed coordination spheres. Cd(II) is placed in the inner N_2O_2 and heavier Pb(II) in the outer O_4 compartments of the de-protonated form of the ligand $[L]^{2-}$. Supramolecular interactions in the intricate crystal structure produced attractive molecular architectures of the compound. The flexible aliphatic –OH pendent group coordinates with the Pb(II) ions. This unique binding further elevates the supramolecular crystal topographies. The supramolecular interactions were authenticated by Hirshfeld surface analysis (HSA). The observation of the recurring unconventional tetrel bonds was rationalized by DFT calculations and surface plots of molecular electrostatic potential (MEP). In the 1D polymeric chain in the complex, the O-atom of the –OH groups shows a tetrel bonding interaction with the Pb atom. We have found that the combination of QTAIM/NCI and QTAIM/ELF plots helps reveal the nature of these contacts. Moreover, the QTAIM/ELF plot determines the donor–acceptor interaction between the O-atom and the Pb atom, establishing the σ-hole. Agreeably, the σ-hole interaction also helps Pb(II) serve as a Lewis acid in the complex. Finally, spodium and tetrel bonds are formed, possible thanks to a hemi-directional coordination sphere of the Pb atoms in the polymer described.

Received 25th December 2021
Accepted 24th January 2022

DOI: 10.1039/d1ra09346k

rsc.li/rsc-advances

Introduction

About a century and a half ago, J. D. van der Waals appeared to be the first scientist to investigate non-covalent interactions in his doctoral dissertation.[1] Since then, non-covalent interactions have proven to be powerful tools for crystal engineering and building supramolecular architectures of coordination compounds that may be discrete or polymeric.[2] The function of non-covalent interactions in present-day chemistry was supported by announcing a series of International Conferences on Non-covalent Interactions (ICNI).[3] Scientists around the world have synthesized a significant number of supramolecular coordination compounds.[4] In addition, polymeric complexes were also formed using Salen-type ligands in association with pseudohalide spacers (Scheme S1†).[5–12] The inner N_2O_2 compartment is very efficient for accepting a 3d metal ion, while the more significant outer O_4, a heavier metal ion (Schemes S2A–S2C†).[13,14] The relevant categories of coordination complexes applications are mainly in bioinorganic chemistry,[15] separations and encapsulation,[16] and bio-relevant catalysis.[17] Also, hydrometallurgy,[18] metal clusters,[19] material science and magnetism,[20] and small molecules transport and activation.[21]

[a]*Department of Chemistry, Tamralipta Mahavidyalaya, Tamluk 721636, West Bengal, India. E-mail: dmajumdar30@gmail.com*

[b]*Department of Chemistry, Indian Institute of Technology (Indian School of Mines), Dhanbad, Jharkhand, 826004, India*

[c]*Department de Quimica, Universitat de les Illes Balears, Cra. de Valldemossa km 7.5, 07122 Palma de Mallorca, Baleares, Spain*

[d]*Department of Basic Sciences, Chemistry Discipline, Institute of Infrastructure Technology Research and Management, Near Khokhara Circle, Maninagar East, Ahmedabad-380026, Gujarat, India*

† Electronic supplementary information (ESI) available. CCDC 2084718. For ESI and crystallographic data in CIF or other electronic format see DOI: 10.1039/d1ra09346k

Within the competence of crystal engineering, scientists are using various non-covalent intermolecular forces. Probably hydrogen bonding, π–π stacking, (an)agostic bonding, cation/anion–π, C–H···π interactions, *etc.* which opened a new area of research.[22] Recently, a unique type of non-covalent interaction has been defined, namely σ-hole bonds,[23–26] and when the group IV elements are involved these are termed tetrel bonds.[27,28] Large and polarizable, heavier Pb(II) is particularly interested in forming tetrel bonds among these group IV elements. Pb(II) can act as an electron donor to include supramolecular interactions. Meanwhile, Pb(II) can present a hemi-directed coordination environment, thanks to a stereo-chemically active lone pair $6s^2$,[29] leading to a significant coordination gap. Tetrel bonding[30] is generally characterized by two different classes of structural organizations, *viz*: holo-directed[31] and hemi-directed[32] geometries (Scheme S3†). In the former case, the bonds of Pb to donor ligand atoms are directed across the surface of an enclosing sphere. In contrast, the Pb bonds to ligand atoms are made across a hemisphere in the latter case. There is a clear gap in the distribution of the bonds to the ligands.[33] These interactions have been widely referred to for chalcogen, pnictogen, and halogen atoms.[33] Nonetheless, relatively little work has researched group IV with tetrel bonding for lead complexes.[34–37] It is well known that the size and electron deficiency of σ-holes increase with the polarizability of the Lewis acid atom.[10] In this context, the importance of the spodium bonding role increases daily, mainly for the d^{10} group of metal ions.[38] Further, the coordination chemistry of Pb(II) is not untouchable. The growing synthesis of Ni(II)/Pb(II) coordination compounds motivates our researchers to look for privileged Pb(II)–Salen complexes. Therefore, in this contribution, we continued our research studies on new Pb(II)-based supramolecular architectures formed through non-covalent interactions, including the tetrel bond. The high atomic number ($Z = 82$), radius adequate to embrace other coordination numbers from 2 to 10 to continue in variable valence states, and skilful coordination chemistry have attracted synthetic inorganic chemists to map unique lead complexes.[39–42] Lead is deadly poisonous[43] and good safe guards must be embraced to prepare its complexes. Most Pb materials are applied in semiconductors, batteries, ferroelectric and non-linear optical materials.[44–49] Moreover, filled d^{10} metal ion (Zn/Cd/Hg) ground states have no significance CFSE, as seen for other d^n electronic systems (n = number of d orbital electrons).[50,51] These factors also helped select cadmium metal for the novel CP formation associated with the lead metal.

This work reports a new structurally characterized CP derived from a compartmental Salen ligand. The spodium and tetrel bonds observed in the solid-state architecture have been analyzed using DFT calculations. The combination of QTAIM/NCI and QTAIM/ELF plots helps to reveal the nature of these contacts. We believe that the findings reported will benefit scientists working in crystal engineering and QTAIM/ELF tools to analyze spodium and tetrel bonds in the theoretical chemistry community.

Experimental section

Materials and measurements

The chemicals and solvents used to synthesize the ligand and CP were reagent grade and were used without further purification. $Cd(OAc)_2 \cdot 2H_2O$, $Pb(NO_3)_2$, sodium thiocyanate (NaSCN), 3-methoxy-2-hydroxybenzaldehyde, and 2-hydroxy-1,3-diaminopropane were purchased from the Sigma Aldrich Company, USA. Elemental analysis (CHN) and mass spectrometry were carried out using a PerkinElmer 2400 CHN elemental analyzer and MALDI-TOF: Bruker Auto flex max LRF. IR and Raman spectra were recorded as KBr pellets (4000–400 cm^{-1}) using a PerkinElmer spectrum RX 1 and BRUKER RFS 27 (4000–50 cm^{-1}) model. ^1H and ^{13}C NMR spectra were collected on a Bruker 400 MHz and 75.45 MHz FT-NMR spectrometer using TMS as an internal standard in DMSO-d_6. BRUKER AXS carried out PXRD measurements and a GERMANY X-ray diffractometer D8 FOCUS model with Cu Kα-1 radiation was used. UV-visible spectra of the ligand (CH_3OH) and the complex (DMF) (200–1100 nm) were determined using a Hitachi model U-3501 spectrophotometer.

Theoretical methods

The calculations reported herein were performed using the Turbomole 7.2 program.[52] The crystallographic coordinates were used for the calculations of the supramolecular assemblies, since we are interested in the analysis of the non-covalent interactions as they stand in the solid state. The level of theory used for the analyses was PB86-D3/def2-TZVP.[53,54] For cadmium and lead, this basis set includes effective core potentials (ECP) and considers relativistic effects for the inner electrons.[55] This level of theory has been used before to evaluate non-covalent interactions in the solid state.[56,57] The MEP surface plots were generated using the wavefunction obtained at the same level of theory and the 0.01 a. u. iso-surface to simulate the van der Waals envelope. The topological approach of the electron density was carried out according to the quantum theory of atoms in molecules (QTAIM) and non-covalent interaction plot index (NCI plot) methods proposed by Bader[58] and W. Yang *et al.*,[59] respectively. Both were represented using the VMD program[60] and using the following settings for the NCI plot index representation: $s = 0.5$ a. u.; cut-off $\rho = 0.04$ a. u., and color scale $-0.04 \leq \text{sign}(\lambda_2)\rho \leq 0.04$ a. u. The electron localization function (ELF)[61] analysis was performed using the MultiWFN program[62] at the PB86-D3/def2-TZVP level of theory. This level of theory has been recently used to analyze similar interactions with ELF.[33d]

X-ray crystallography

Light yellow crystal complexes were grown after slow evaporation of the methanol solvent in the presence of a few drops of acetonitrile. We have selected 3–4 good quality crystals with microscopic observation for crystal data processing purposes. The crystal data for the CP were collected on a Bruker CCD[63] diffractometer using Mo Kα radiation at $\lambda = 0.71073$ Å. We have used several different crystallographic programs. SMART is used for accumulating frames of information, indexing

reflections, and determining lattice parameters, SAINT[64] for the combination of the intensity of reflections, and scaling, SADAB[65] for absorption correction, and SHELXTL for space group, structure determination, and least-squares refinements on F^2. The crystal structure was solved using full-matrix least-squares methods against F^2 using SHELXL-2014 (ref. 66) and Olex-2 software.[67] All the non-H atoms were refined with anisotropic displacement parameters, and all hydrogen positions were constant at calculated positions, which can be delicate iso-tropically. An overview of the crystallographic information and complete structure refinement parameters are shown in Table 1.

Synthesis of ligand (H_3L)

After suitable modification, the Salen-based ligand has been synthesized following the literature method (Scheme 1).[68] The reflux condensation of 3-methoxy-2-hydroxybenzaldehyde (0.152 g, 1 mmol) with 2-hydroxy-1,3-diaminopropane (0.0451 g, 0.5 mmol) in (50 mL) methanol at 60 °C for 3 h prepared H_3L. Under vacuum, the solvent was removed. The yellow crystal solid product separated upon cooling, and the product was air-dried. Yield: 0.212 g (85.2%), anal. calc. for $C_{19}H_{22}N_2O_5$: C, 63.67; H, 6.19; N, 7.82 found: C, 63.62; H, 6.24; N, 7.84%. IR (KBr cm^{-1}) selected bands: ν(C=N) 1662 vs, ν(C–$O_{phenolic}$) 1238 vs, ν(O–H) 3220 m. ^{1}H NMR (DMSO-d6, 400 MHz): δ (ppm): 3.83–3.86 (s, $3H^1$), 4.08 (1H, aliphatic –OH^8), 7.37–7.38 (m, $1H^2$–H^4), 8.65 (m, $1H^6$), 13.91 (m, $1H^5$), 3.32–3.77 (s, $2H^7$) (Scheme S4†). ^{13}C NMR (DMSO-d6, 75.45 MHz): δ (ppm): 55.19–67.69 (O–$^1CH_3$), 106.12–132.93 (Arom-^{3}C–^{5}C), 152.26 (^{7}C–OH), 168.40–172.62 (^{8}CH=N). UV-vis λ_{max} (CH_3OH): 380 nm.

Synthesis of $[(Cd)(Pb)(L)(\eta^1\text{-NCS})(\eta^1\text{-SCN})]_n$ (1)

$Cd(OAc)_2 \cdot 2H_2O$ (0.219 g, 1 mmol) was dissolved in 25 mL of hot methanol. Then a methanolic solution of H_3L (0.359 g, 1 mmol) was added, followed by the drop-wise addition of an aqueous methanolic solution of NaSCN (0.081 g, 1 mmol). The resultant mixture was refluxed at room temperature for 2 h. Then, ten drops of methanol solution of $Pb(NO_3)_2$ (0.331 g, 1 mmol) were added to this reflux solution. The mixture was stirred at 75 °C for 1 h. Finally, a few drops of acetonitrile (ACN) were poured into this refluxed solution under ice-cooled conditions. The light-yellow solution was filtered and stored under refrigeration for crystallization. After a few days, block-sized, light yellow-coloured single crystals were obtained, suitable for SCXRD. Crystals were isolated by filtration and air-dried. Yield: 0.418 g, (57%), anal. calc. for $C_{21}H_{20}CdN_4O_5PbS_2$: C, 31.84; H, 2.54; N, 7.07. Found: C, 31.80; H, 2.51; N, 7.09%. MALDI-TOF MS: MW (792.12), m/z = 791.82 (Fig. S1†). FT-IR (KBr cm^{-1}) selected bands: ν(C=N) 1616 s, ν(NCS) 2087 s, ν(SCN) 2173 m, ν(Ar–O) 1355 s. FT-Raman (cm^{-1}) selected bands: ν(C=N) 1632 s, ν(NCS) 2116 s, ν(SCN) 2199 m. ^{1}H NMR (DMSO-d6, 400 MHz): δ (ppm): 3.30 (s, $3H^1$), 7.15 (m, H^2–H^4), 8.31 (w, $1H^6$), 3.89 (m, $2H^2$), 3.26 (s, $6H^7$). UV-vis λ_{max} (DMF): 296 and 326 nm.

Table 1 Crystal data and structure refinement parameters

Formula	$C_{21}H_{20}CdN_4O_5PbS_2$
M/g	792.12
Crystal system	Monoclinic
Space group	$P2_1/c$
a/Å	9.813(7)
b/Å	16.798(12)
c/Å	15.066(11)
α (°)	90
β (°)	97.022(9)
V/Å^3	2465(3)
Colour	Pale yellow
Z	4
ρ_c/g cm^{-3}	2.135
μ/mm^{-1}	7.894
F (000)	1504
Cryst size (mm^3)	0.078 × 0.054 × 0.033
θ range (deg)	2.42 to 17.41
Limiting indices	$-11 \le h \le 11$
	$-20 \le k \le 20$
	$-18 \le l \le 18$
Reflns collected	59 792
Ind reflns	4584 [R_{int} = 0.1269, R_{sigma} = 0.0565]
Completeness to θ (%)	0.999
Refinement method	Full-matrix-block least-squares on F^2
Data/restraints/parameters	4584/0/310
Goodness-of-fit on F^2	1.033
Final R indices	R_1 = 0.0436
[$I > 2\sigma(I)$]	wR_2 = 0.0935
R indices (all data)	R_1 = 0.0710
	wR_2 = 0.1075
Largest diff. peak and hole (e Å^{-3})	0.755 and −1.466

Results and discussion

Synthetic rationalization

The Salen ligand was synthesized using the previously reported literature method (Scheme 1).[68] CP derived from H_3L and thiocyanate spacer was prepared in moderate good yield by selecting the more familiar self-assembly *in situ* procedure (Scheme 1). The synthesized CP is insoluble in water and the most common organic solvents. The heteronuclear CP has good thermal stability. The synthetic method was repeated by adding Cd(II) and then Pb(II). All cases had Cd(II) occupying the inner N_2O_2 and Pb(II) occupying the outer O_4 cavities probably due to the larger size of Pb(II), whose ionic radius (133 pm) is much larger than that of Cd(II) (109 pm).[10,49] The single crystals were not grown in methanol solvent alone; hence, we used a few drops of acetonitrile to promote better diffracting-quality crystals suitable for SCXRD (Scheme 1). Salen encompasses two imines, two phenols, two alkoxys, and one weakly acidic aliphatic –OH group. After deprotonation, the reference salen always produces an N_2O_2 imine chelating position.[68] Herein, the flexible aliphatic –OH pendent group played a significant role in constructing supramolecular self-assembly through hydrogen bonding. H_3L has displayed only a few examples of heteronuclear compounds in the absence of pseudohalides.[68] So far, CPs with the flexible –OH pendent group coordinated with Pb(II) ions in the presence of a thiocyanate spacer are scarce in the literature. The σ-hole type interaction and spodium/tetrel bonding concept verified using DFT studies confirm our synthesized CP is novel.

Spectroscopic characterization

IR/Raman spectroscopy was used to characterize the Salen and the coordination polymer. The ligand's identified imine (C=N) stretching vibration came near 1662 cm^{-1} (Fig. S1A†).[69] The mass is determined using the BRUKER MALDI-TOF and corresponds to the molecular weight of the CP. For the complex, the stretching vibration bands for IR and Raman (C=N) are shifted to 1616 cm^{-1} (Fig. S1†) and 1632 cm^{-1} (Fig. S2†). These spectral data support the coordination mode of the azomethine nitrogen atom to the Cd metal centre.[70] Thiocyanate ligands (SCN^-) displayed two strong bifurcated bands at 2087, 2173 cm^{-1} (**1**) (IR) and 2116, 2199 cm^{-1} (**1**) (Raman). Such splitting patterns are attributed to two distinct binding modes with the Cd and Pb metal ions.[71] The Ar–O stretching frequency near 1239 cm^{-1} is identical with reported salen-type ligands. The UV-vis absorption spectra of the salen and the CP were analyzed in CH_3OH and DMF. The ligands exhibit bands at 380 nm (Fig. S3†) for $\pi \rightarrow \pi^*/n \rightarrow \pi^*$ type transitions. In contrast, the CP reveals a potent ligand-based UV domain at 296, 326 nm (Fig. S4†) due to the L → M charge-transfer transition ($\pi \rightarrow \pi^*/n \rightarrow \pi^*$).[70,72] The spectra mentioned above are identical to the previously reported Salen.[73,74] The UV spectral-domain supports the coordination mode of the Salen ligand with Cd and Pb ions. Due to the d^{10} configuration and the Cd(II) diamagnetic nature, no metal-centered broad d–d absorption band has been identified. The NMR spectra ($^1H/^{13}C$ NMR) characterized the Salen and the CP (Fig. S5–S7†). Free Salen in the region δ 5.0–8.0 ppm did not show a broad peak, indicating the absence of the $-NH_2$ group. The NMR peak value at δ 4.08 ppm was identified as the $-OH^8$ aliphatic proton. The phenolic protons (OH^5) are associated with the defined broad peak at δ 13.91 ppm. The protons (H^6) attached to the imino carbon are downfield shifted δ 8.65 ppm[73,74] due to the influence of the combined effect of phenolic –OH and imino N groups in close vicinity. The peaks within the range δ 7.37–7.38 ppm correspond to the aromatic protons (H^2–H^4). The three methyl protons ($OCH^1{}_3$) attached to the aromatic oxygen appear at δ 3.83–3.86 ppm. Due to the difficult solubility of the CP in DMSO-d6, the result of the ^1H NMR spectrum is not satisfactory. In the case of the CP, the coordination mode of the azomethine nitrogen was assigned by the downfield shift of the azomethine proton signal from the ligand. The OH proton (OH^5) signal at the ligand disappeared in the ^1H NMR spectrum of the complex, showing deprotonation and coordination of the O-atom with Cd metal ion.[73,74] Further, the ^{13}C NMR spectrum of the ligand showed the azomethine (CH=N) carbons at 168.40–172.62 ppm, 55.19–67.69 (O–CH_3), 106.12–132.93 (Arom-C), 152.26 (C–OH) ppm (Fig. S6†).

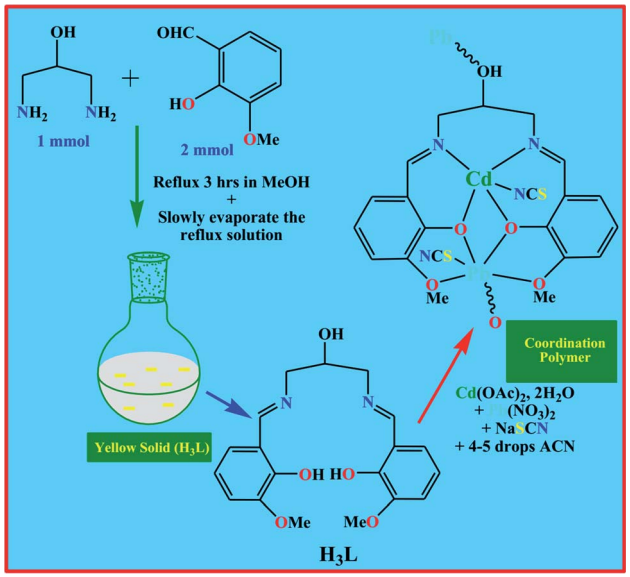

Scheme 1 Synthetic strategy for H_3L and the coordination polymer.

SEM-EDX mapping and PXRD

The EDX experiment has successfully determined the elementary composition of the CP. The chemical composition has correctly confirmed the presence of Cd and Pb metal ions in the EDX profile. The EDX profile of the CP is shown in ESI 2.† Thus, the empirical formula of the CP is fully justified. The EDX profile reflects the highest peak as Pb, followed by Cd metal ions. We have further performed EDX elemental mapping, a qualitative analysis method: high concentrations of an element of interest appear as a light contrast in the map, low concentrations result in dark contrast (ESI 3†). Further, SEM supports the structural and morphological features. SEM

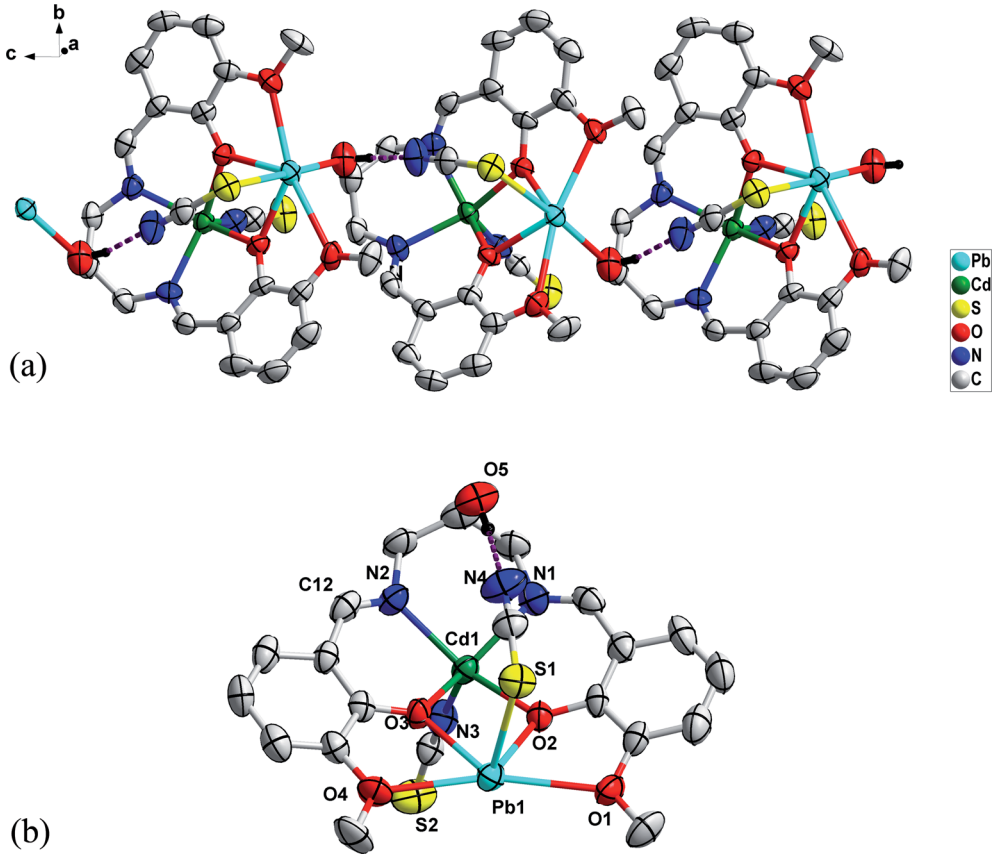

Fig. 1 (a) Molecular structure of 1D polymeric chain of **1**; intramolecular H bonding is shown as violet dotted lines. Other H atoms have been omitted for clarity. (b) Asymmetric unit of complex **1**.

images characterized the size and morphological structure of the prepared complex. The SEM micrograph directly supports the morphology of the complex plate shape. The PXRD method studied the phase purity and crystallinity, and the recorded diffraction patterns were at room temperature. Experimentally scanning the compound in the range ($2\theta = 40$–50°) recorded the PXRD patterns. The well-defined sharp PXRD peaks support the crystalline nature of the CP (Fig. S8†). The experimental and simulated PXRD patterns of the material match well, indicating the consistency of the bulk sample.

Crystal structure of $[(Cd)(Pb)(L)(\eta^1\text{-NCS})(\eta^1\text{-SCN})]_n$ (1)

X-ray single-crystal data analysis reveals that the compound crystallizes in the monoclinic system in the $P2_1/c$ space group ($Z = 4$). A perspective view of **1** is depicted in Fig. 1a. Selected bond parameters related to the CP are summarized in Table S1.†

The asymmetric unit of **1** (Fig. 1b) consists of a hetero-bimetallic core containing full occupancy Cd(II) and Pb(II) metal ions, one fully deprotonated equatorial $[L]^{2-}$ and two axial $[SCN]^-$ spacers. In the asymmetric unit, partially deprotonated ligands consist of two pockets. These are the inner N_2O_2 pocket (two imine N atoms, phenolate O atoms) and outer O_4 pockets (two phenolate O atoms, O atoms from –OMe groups) (Scheme S2A–S2C†). The inner and outer pockets accommodate Cd1 and Pb1 centers, respectively which are connected by two bridging deprotonated phenoxide O atoms in μ_2 fashion to construct the hetero-bimetallic $[Cd(O_2)Pb]$ core. The competitive occupation of Cd(II) *vs.* Pb(II) is one of the most exciting aspects of the stereochemistry, Cd(II) occupies the inner N_2O_2, and Pb(II) occupies the outer O_4 compartments. The significant Pb(II) ionic radius (133 pm) is much larger than that of Cd(II) metal ions (109 pm). It is difficult for Pb(II) to be accommodated in the inner N_2O_2 compartment, where the Cd(II) fits well with the outer O_4 cavities. Therefore, the Pb(II) ion resides well in the open external O_4 pit.[10,49] Interestingly, in this *modus operandi* of thiocyanate, the Pearson theory holds very well.[49] Between Cd(II)

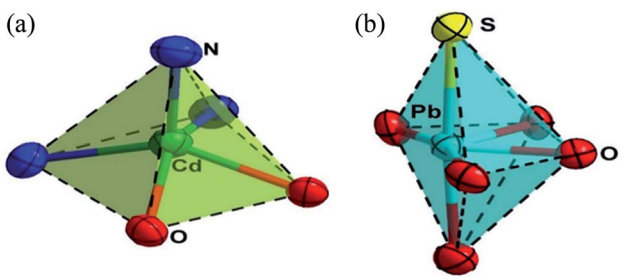

Fig. 2 (a) Distorted square pyramidal geometry around Cd1. (b) Distorted octahedral geometry around Pb1.

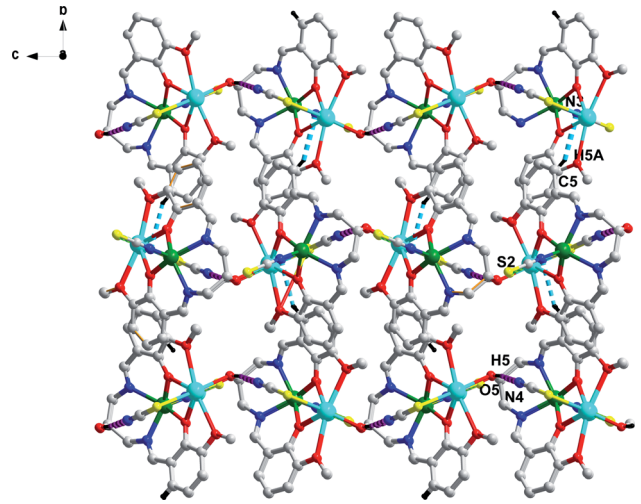

Fig. 3 2D-hydrogen bonded network along the *ab* plane of **1**.

and Pb(II) ions, the former is a hard acid, and the latter is a soft acid. Thus, the sulfur atom (soft base) of thiocyanate is preferably linked to the soft acid Pb(II), and the nitrogen atom (hard base) is associated with the hard acid Cd(II) ion. Further studies of the Cambridge Structural Database (CSD) (Fig. S9†) confirmed the preferred thiocyanate N-bonded bonding with d^{10} Cd(II) metal ions.[43] The Cd–Pb distance within the four-membered ring is 3.691(2) Å with a Cd–O–Pb angle of 104.86(7)°. Besides the binding provided by $[L]^{2-}$, the dinuclear complex is further supported by the coordination action of two thiocyanate ligands. The thiocyanate ligands function as monodentate ligands satisfying the coordination number of the metal centers. The ligand also balances the overcharge of the molecule. Interestingly, the Cd(II) and Pb(II) centers coordinated to terminal thiocyanate κN-SCN and κS-SCN ligands. The Addison structural parameter (τ)[75] value helps to determine the stereochemical environment around the Cd(II) ions, ($\tau = (\beta - \alpha)/60°$ where β and α are the two largest angles around the central atom: $\tau = 0$ for perfect square pyramidal and 1 for an ideal trigonal geometry). The Cd center has a distorted square pyramidal geometry (Fig. 2) with a τ value of 0.046. The apical position is occupied by an N atom from the thiocyanate anion and the basal plane consists of N_2O_2 donors from $[L]^{2-}$. On the other hand, the Pb center displays a distorted octahedral coordination geometry with six bond pairs and a lone pair where hemi-directed coordination geometry is observed around the Pb center (Fig. 2). The basal plane is occupied by the O_4 donor set from $[L]^{2-}$ and the axial positions are occupied by a N atom from the thiocyanate anion and a hydroxyl group from a neighbouring complex (O5). The lone pair is situated at the "cap" position, distorting the octahedron system (Scheme S5†).

In this complex, lead is in the +2 oxidation state and one of the post-transition elements with total electronic configuration [Xe] $4f^{14}5d^{10}6s^2$ and displaying an inert-pair effect. The $6s^2$ electrons are inert to participate in the oxidation state process/covalent bond formation. They behave as a lone pair which causes the non-spherical charge allocation around the lead ion, *i.e.*, the distribution of ligands around the lead leaves some vacant space (identifiable void). Thus, the lead(II) preferred hemi-directed coordination over the holo-directed coordination sphere.[76–79] The hemi-directed coordination sphere is comparable to previously reported X-ray characterized lead(II) complexes (Table S2†). The coordination of the hydroxyl group from an adjacent complex results in forming a unique hetero-bimetallic one-dimensional (1D) polymer.

The metric parameters reveal that the average bond lengths of $Cd–O_{phenolate}$ and $Pb–O_{phenolate}$ are 2.238 Å and 2.395 Å, respectively. The average bond length of $Pb–O_{methoxy}$ is 2.745 Å which is moderately longer than the $Cd/Pb–O_{phenolate}$ bond. The average bond length of $Cd–N_{imine}$ is 2.252 Å which is slightly larger than the $Cd–N_{thiocyanate}$ bond length of 2.212 Å. The $Pb–S_{thiocyanate}$ bond length is 2.882 Å which is larger than the $Cd–N_{thiocyanate}$ bond length. The solid-state structure of **1** displayed both intra and intermolecular supramolecular interactions. The one-dimensional (1D) coordination polymer itself contains strong intramolecular O–H (alkoxy oxygen)···N (terminal S coordinated thiocyanate ligand) hydrogen bonding with the distance of 1.998 (9) Å. Each 1D coordination polymer interacts with four neighbouring 1D polymers through C–H···N hydrogen bonding forming a 2D-hydrogen bonded network along the *ab* plane (Fig. 3 and Table 2). Apart from H-bonding interactions, the hemi-directed coordination modes around the Pb centre allow them to establish σ-hole interactions with lone pairs from S atoms.[23–28] From a topological point of view, the 1D coordination polymers are further connected by Pb···S tetrel bonds (Fig. 3). The Pb···S contact distance is 3.337 Å which is longer than the sum of the covalent radii and shorter than the sum of the van der Waals radii, and it is comparable with the previous literature reported Pb···S contact (Table S3†). We have also accomplished theoretical analysis of **1** in the crystal structures to advance further insight into the interactions that hold them together.

A novel X-ray crystal structure: comparison with analogous complexes

The coordination chemistry of the flexible, weakly acidic aliphatic –OH group appending Salen ligand (H_3L) is limited in the literature.[68] There are some examples of literature published heteronuclear complexes using H_3L, especially in the absence of the thiocyanate spacer, such as $[Cu(HL)Na(NO_3)(MeOH)]$, $[Cu(HL)Hg(Cl)_2]$, $[Cu(HL)Zn(NO_3)(H_2O)]NO_3$, $[Cu(HL)(H_2O)$

Table 2 Non-covalent interaction geometry (Å) for complex

D–H	*d*(D–H)	*d*(H···A)	<DHA	*d*(D···A)	A	Symmetry code
O5–H5	0.82(6)	1.998(9)	158.83(5)	2.783(11)	N(4)	$x, 1.5 - y, -0.5 + z$
C5–H5A	0.92(9)	2.746(8)	147.18(5)	3.563(12)	N(3)	$x, 1 + y, -1 + z$

$Sm(NO_3)_3$], [Cu(HL)(H_2O)Bi(NO_3)$_3$], [Cu(HL)Pb(NO_3)$_2$], and [Cu(HL)Cd(NO_3)$_2$]. We envisioned introducing a flexible aliphatic hydroxyl group into such a salen to check the improvement of the H-bonding ability of the resulting CP, or it could be coordinated with metal ions such as Pb(II). It controls the crystal structural features and dimensionality in the resulted solids. Our goal is to determine if the –OH group remains uncoordinated with the metal ions or is involved in H-bonding. Thereby generating supramolecular architectures expanding from discrete to a 3D network. We observed most of the complexes without using thiocyanate spacers. Our complex is 1D hetero-binuclear CP made in the presence of sodium thiocyanate. Meanwhile, the X-ray crystal structure shows that heavier Pb(II) ions in our CP are coordinated with the ligand's weakly acidic –OH group, which explains its novelty. The activity attached to the –OH group leads to the formation of a 1D CP. In addition, all previously published heteronuclear complexes' internal and external compartments have a common occupancy, but our prepared CP highlighted two different compartment occupancies. There are five coordinated distorted square bipyramidal geometries around Cd metal ions and a hemi-directed coordination sphere around the lead. Another remarkable feature of the reported complexes described is that the ligand can take up all additional metal ions in an open O_4 compartment quite comfortably, regardless of the size and charge of the ions, which demonstrates the flexibility of the ligand.[68] The radius factor governs the 2nd Pb metal ion's accommodation at the external O_4 compartment in our complexing system. The reported complexes show only usual non-covalent interactions, *e.g.*, H-bonding, π–π, and C–H–π stacking, responsible for understanding possible supramolecular topologies. Interestingly, our 1D polymeric network undergoes several non-covalent interactions (S···H, C–H···π and hydrogen bonding) to form a 2D grid. However, a significant difference was observed for the overall composition of the previously reported complexes, where non-appending of –OH groups leads to mononuclear or discrete complexes, contrary to the present CP. Moreover, the synthesized CP shows unconventional σ-hole type interactions, and spodium and tetrel bonding features. The above discussion thoroughly investigates the synthesized CP possessing a new crystal structure and –OH groups with pendent supramolecular topologies.

Hirshfeld surface analysis

The role of the flexible aliphatic –OH groups in the salen is directed towards self-organization in the crystal structure. The supramolecular topologies are correlated with the HSA mapping.[80] The hydrogen bonds were considered the possible supramolecular topologies. HSA was performed with the Crystal Explorer 17.5 software.[81] The calculations were evaluated using the complex*.cif extension file. For each point on the Hirshfeld surface (HS), two distances are defined: d_e, the distance from the point to the closest nucleus external to the surface; and d_i, the distance to the nearest nucleus internal to the surface. The normalized contact distance (d_{norm}) based on d_e and d_i is given by $d_{norm} = d_i - r_i^{vdw}/r_i^{vdw} + d_e - r_e^{vdw}/r_e^{vdw}$, where r_i^{vdw} and r_e^{vdw} are the van der Waals radii of the atoms. If the d_{norm} is negative, the intermolecular contact is expected to be shorter than r^{vdw}. On the other hand, if the d_{norm} is positive, it is expected to be longer. Usually, d_{norm} displays a surface with a red, white and blue colour contour map, with bright red spots highlighting shorter contacts, white areas representing contacts around the van der Waals separation, and blue regions not having close contacts.[28b] The HS using the standard Tonto code shows the intermolecular interactions exhibited at the Cd–S and Pb–O bonding. Interestingly, Pb and Cd atoms are not involved in any intermolecular interactions. The van der Waals interaction between the C–H is the highest among S–H interactions (Table 3). The total volume of the surface is 606.29 Å^3, globularity is

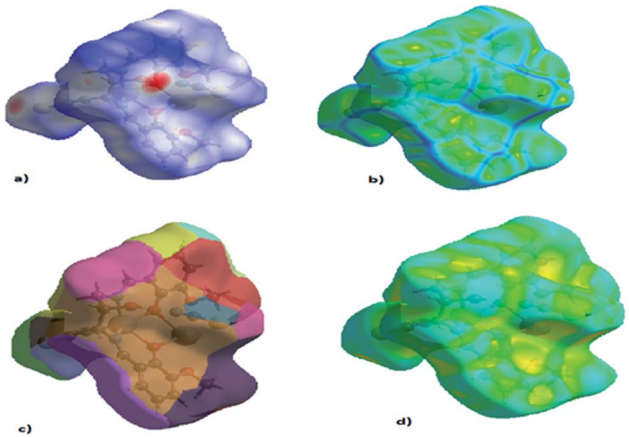

Fig. 4 HSA mapped for the CP: (a) d_{norm}, (b) curvedness, (c) fragment patch, (d) shape index.

Table 3 HSA based different intermolecular interactions

Types of intermolecular interactions	Percentage contribution (%)
H-bond (O and outside H)	5.9
H-bond (S and outside H)	16.7
H-bond (N and outside H)	9.7
π–π stacking	2.7
C–H weak interactions	23.8

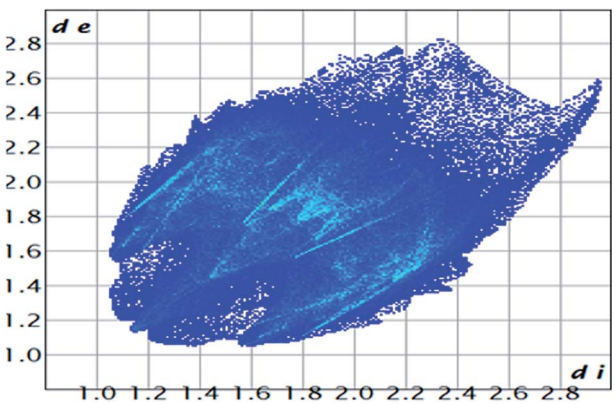

Fig. 5 2D HS plot showing different types of interactions.

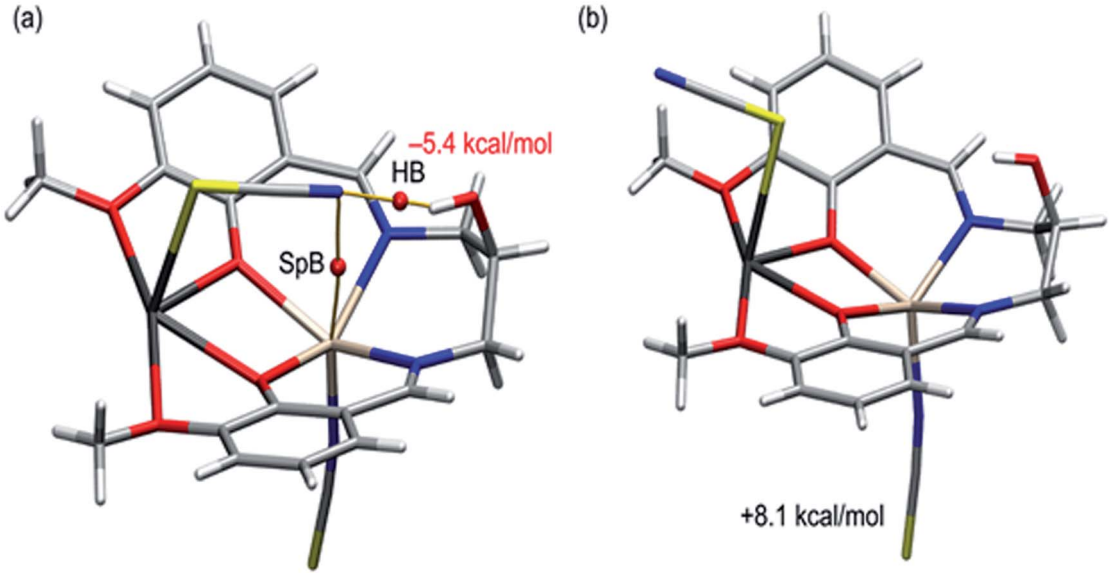

Fig. 6 (a) QTAIM distribution of bond critical points and bond paths involving the non-coordinated N-atom of the pseudohalide. The rest of the bond critical points and bond paths are omitted for clarity. (b) Theoretical model where the thiocyanate ligand coordinated to Pb has been rotated.

0.718, and the asphericity is 0.028. Hence the complex deviates from the perfect spherical shape, and the mean curvedness of the complex is −0.9834. Fig. 4 and 5 show the complete 2D fingerprint plot of the CP.

QTAIM approach: spodium bond

We have first studied the conformation adopted by the thiocyanate ligand coordinated to the Pb metal center. The N-end of the SCN ligand establishes two non-covalent interactions: a hydrogen bond with the hydroxyl group and a spodium bond (SpB) with the Cd(II) atom. The latter interactions have been recently studied in penta-coordinated Zn-atoms, demonstrating their importance in crystal engineering.[82] Fig. 6a shows the complex's QTAIM analysis (bond critical points represented as red spheres). A bond critical point can be observed that connects the N-atom to the H-atom, thus confirming the existence of the interaction. The energy associated with this contact has been computed using the potential energy density value at the bond critical point (V_r) and the equation proposed by Espinosa *et al.* ($E_{dis} = -0.5 \times V_r$).[83] As a result, the H-bond energy is −5.4 kcal mol^{-1}, confirming its importance in influencing the SCN orientation. To estimate the contribution of the SpB, we have also computed a theoretical model where the SCN has been rotated (Fig. 6b) and, consequently, the intramolecular hydrogen bonding and SpB are not established. This hypothetical model is 8.1 kcal mol^{-1} less stable than the experimental conformation; thus, the spodium bond's contribution is −2.7 kcal mol^{-1} in line with previous investigations.[84]

MEP and QTAIM/NCI plot: tetrel bond

Fig. 7a shows the 1D polymeric chain observed in the solid-state of the complex where the O-atom of the hydroxyl groups forms a tetrel bonding (TtB) interaction with the Pb(II) atom. The Pb⋯O distance is 2.782 Å, which is longer than the sum of the covalent radii ($\Sigma R_{cov} = 2.12$ Å) and much shorter than the sum of the van der Waals radii ($\Sigma R_{vdw} = 3.54$ Å). Moreover, the Pb⋯NCS–Cd distance is 3.62 Å, which is slightly longer than the $\Sigma R_{vdw} = 3.57$ Å, which is indicative of weak van der Waals interactions. The MEP surface of the complex is represented in Fig. 7b. The most nucleophilic part is located at the negative belt of the S-atom belonging to the coordinated Cd–thiocyanate. The MEP is also large and negative at the O-atom of the hydroxyl group (−36 kcal mol^{-1}). The MEP maximum is located at the Pb atom (equatorial plane). The MEP values are also large and positive at the H-atoms of the methoxy groups and the Pb-atom opposite to the Pb–S bond (σ-hole). The QTAIM/NCI plot analysis of a dimer extracted from the 1D supramolecular chain is shown in Fig. 7c. In this representation, only the intermolecular interactions are depicted. The distribution of bond critical points and NCI plot index iso-surfaces shows the existence of several interactions, mostly CH⋯π (pseudohalide). This type of contact has been described before in X-ray structures.[85] Remarkably, the QTAIM analysis confirms the existence of two tetrel bonds (Pb⋯O, N), characterized by the corresponding bond critical points and bond paths interconnecting the Pb atom to the O, N-atoms. The blue and green colors of the NCI plot iso-surfaces that characterize the Pb⋯O and Pb⋯N interactions, respectively, reveal that the Pb⋯O is stronger, in line with the shorter distance. The dimerization energy is very large ($\Delta E = -34.7$ kcal mol^{-1}) because of the intricate combination of interactions, as evidenced by the number of bond critical points and bond paths connecting both monomers. To evaluate the contribution of the Pb⋯O tetrel bond (TtB), we have used a mutated model where an H-atom has replaced the OH. Consequently, the Pb⋯O tetrel bond is not formed, and the

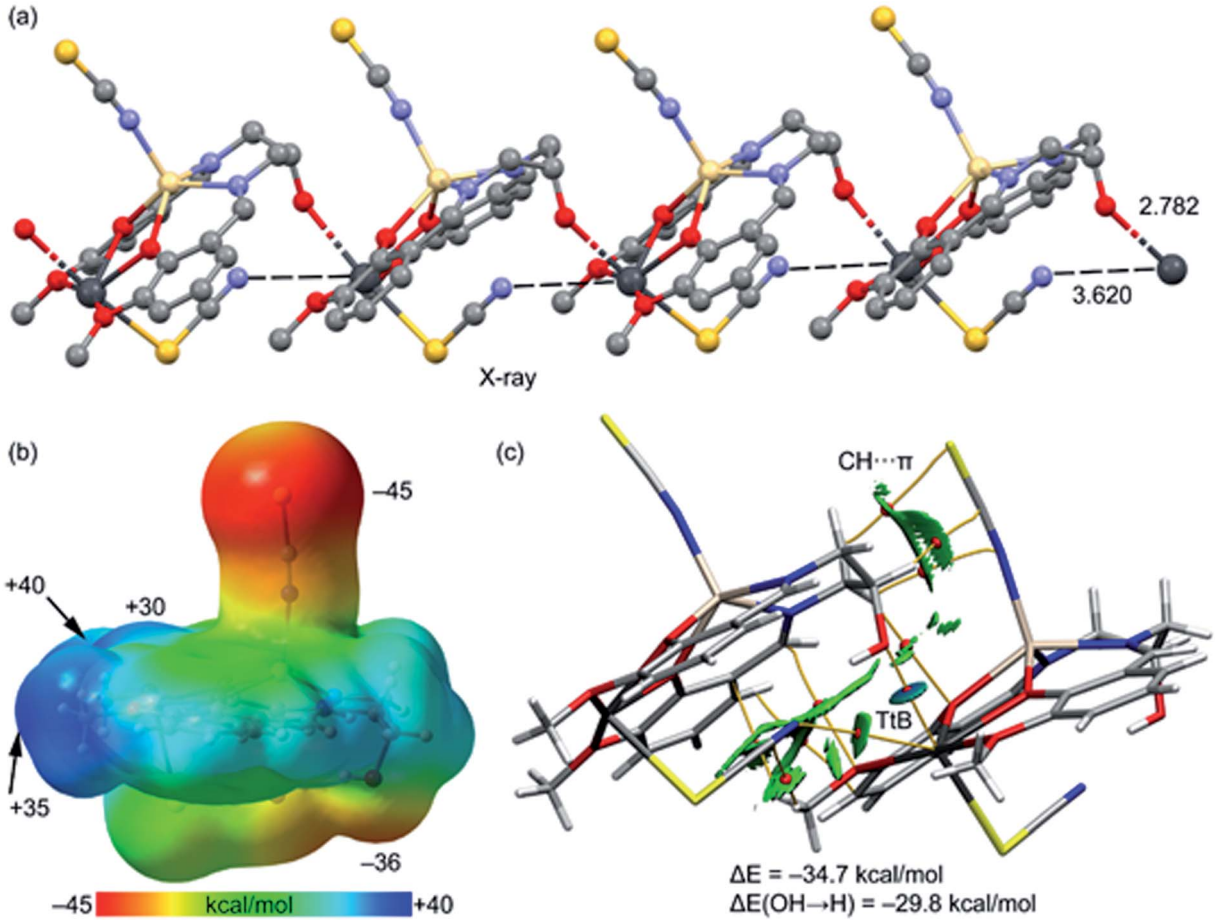

Fig. 7 (a) Partial view of the X-ray structure showing the 1D supramolecular assembly (distances in Å). (b) MEP surface of the complex at the BP86-D3/def2-TZVP level of theory. Iso-surface used 0.01 a. u. The MEP values at selected points of the surface are given in kcal mol^{-1}. (c) Combined QTAIM (bond critical points in red and bond paths as orange lines) and NCI plot index (RDG = 0.5, ρ cut-off = 0.04 a. u., color range: $-0.04 \leq \text{sign}(\lambda_2)\rho \leq 0.04$ a. u.).

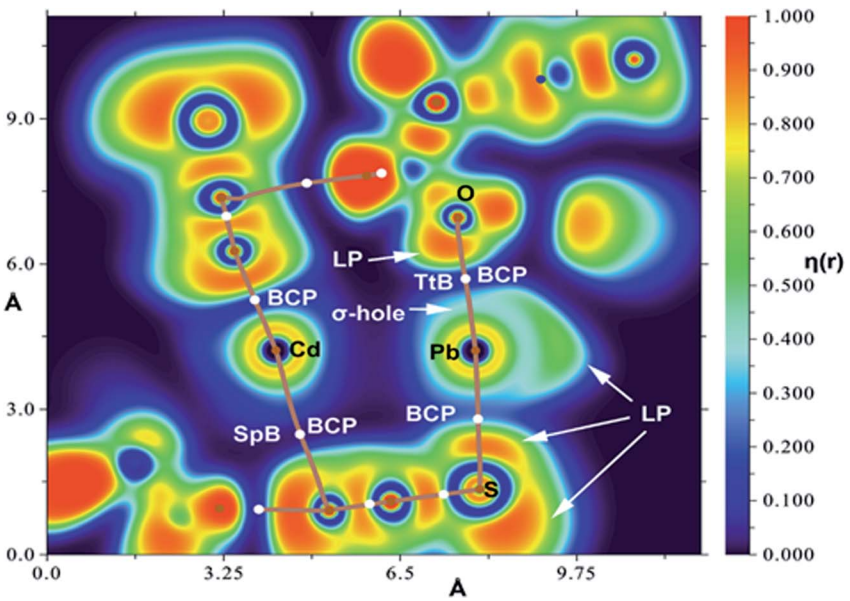

Fig. 8 2D map of the $\eta(r)$ function for the dimer of the complex. The molecular plane corresponds to that defined by S–Pb···O atoms. Bond critical points (BCPs) are represented in white.

interaction energy is reduced to $\Delta E(\mathrm{OH} \rightarrow \mathrm{H}) = -29.8$ kcal mol^{-1}. Thus, the contribution of the Pb···O TtB is roughly estimated by the difference, which is -4.9 kcal mol^{-1}. This moderately strong energy confirms the non-covalent nature of this contact. Further evidence of the non-covalent nature of the Pb···O contact is obtained by the QTAIM parameters at the bond critical point. The positive values of the Laplacian ($\nabla^2\rho = 7.35 \times 10^{-2}$ a. u.) and total energy density ($H_r = 1.56 \times 10^{-4}$ a. u.) at the bond critical point confirm the non-covalent nature of the Pb···O since coordination bonds are characterized by positive values of $\nabla^2\rho$ and negative values of H_r.[86]

QTAIM/ELF model: σ-hole interactions

Finally, we have used the electronic localization function (ELF) combined with QTAIM to analyze the donor–acceptor interaction between the O-atom and the Pb atom and confirm the σ-hole interaction. It has been used to differentiate chalcogen and pnictogen bonds in stibanyl telluranes.[33d] The ELF representation has been performed for the dimer shown above (Fig. 7c). Precisely, the plane used for the ELF topographical 2D map of the $\eta(r)$ function representation corresponds to that defined by the atoms that participate in the S–Pb···O contact, see Fig. 8. The examination of the localization domains corresponding to the lone pairs and σ-hole regions reveals that in the TtB the negative lone pair of O interacts with the lead's σ-hole. The lone pair of lead points perpendicular to the Pb···O vector confirming the σ-hole nature of the interaction, where the Pb is acting as a Lewis acid. Regarding the Pb–S coordination bond, the lone pair's size at the S-atom that points toward the Pb atom is significantly smaller than the other lone pair, as expected upon forming a coordination bond.

Conclusion

This article describes the synthesis, spectroscopic findings, MALDI-TOF, PXRD, SEM, EDX mapping, and single-crystal X-ray characterization of a new 1D heteronuclear Cd(II)/Pb(II) coordination polymer. The X-ray results revealed Cd(II) and Pb(II) metal ions fulfilled distorted square pyramidal and hemi-directed coordination spheres. Cd(II) being placed in the inner N_2O_2 and heavier Pb(II) in the outer O_4 compartments of the deprotonated form of ligand $[L]^{2-}$. The solid-state structure displayed intra- and intermolecular supramolecular interactions. Here the ligand's flexible aliphatic –OH pendent groups uniquely coordinate with the Pb(II) ions. This binding feature further increases the supramolecular crystal topographies. HSA authenticated the supramolecular interactions, and DFT and molecular electrostatic potential (MEP) surface plots showed the CP's recurrent σ-hole interactions/spodium/tetrel bonding. The tetrel bond (-4.9 kcal mol^{-1}) is stronger than the spodium bond (-2.7 kcal mol^{-1}). In addition, coordination bonds (covalent character) and tetrel bonds (non-covalent character) of the complex were differentiated using the quantum concept of "atoms-in-molecules" (QTAIM) and the non-covalent interaction index (NCI index). We found that combining the QTAIM/NCI and QTAIM/ELF plots helps uncover the nature of these contacts. Herein we anticipate that the findings reported will be helpful to scientists working in crystal engineering and the application of QTAIM/ELF tools to analyze spodium and tetrel bonds in the theoretical chemistry community.

Author contributions

Dhrubajyoti Majumdar was the project's primary author and conceived the whole research idea, performed data curation, conceptualization, methodology, research investigation, software visualization, writing review, initial draft preparation, and editing. A. Frontera and Rosa M. Gomila have performed all DFT-based experiments. Sourav Das and Kalipada Bankura were involved in X-ray structure analysis of single crystals and various graphics preparation. All authors in the manuscript carefully read and approved the final version before submission.

Conflicts of interest

The authors do not indicate any competing interests or personal relationships that may have influenced the work reported in this paper.

Acknowledgements

This research has not received specific funding from any funding agency in public, commercial or not-for-profit sectors. All authors thank the Central Laboratory of Tamralipta Mahavidyalaya, Tamluk, West Bengal, India, funded by the DST-FIST Project (Level-0) under the Dept. of Science and Technology, Govt. from India. The corresponding author Dhrubajyoti Majumdar mainly thanks Dr Abdul Motin, principal of Tamralipta Mahavidyalaya, who provided the research laboratory for carrying out the research work.

References

1 J. D. van der Waals, Doctoral Dissertation, University of Leiden, 1873.
2 K. T. Mahmudov, M. N. Kopylovich, M. F. C. Guedes da Silva and A. J. L. Pombeiro, *Coord. Chem. Rev.*, 2017, **345**, 54–72.
3 ICNI 2019, 1st International conference on noncovalent interactions, 2–6 September 2019, https://icni2019.eventos.chemistry.pt/.
4 (*a*) S. Roy, A. Bhattacharyya, S. Purkait, A. Bauzá, A. Frontera and S. Chattopadhyay, *Dalton Trans.*, 2016, **45**, 15048–15059; (*b*) S. Hazra, R. Koner, M. Nayak, H. A. Sparkes, J. A. K. Howard and S. Mohanta, *Cryst. Growth Des.*, 2009, **9**, 3603–3608; (*c*) S. Sasmal, S. Majumder, S. Hazra, H. A. Sparkes, J. A. K. Howard and S. Mohanta, *CrystEngComm*, 2010, **12**, 4131–4140; (*d*) S. Bhattacharya, S. Mondal, S. Sasmal, H. A. Sparkes, J. A. K. Howard, M. Nayak and S. Mohanta, *CrystEngComm*, 2011, **13**, 1029–1036.
5 (*a*) A. Bhattacharyya, M. Das, A. Bauzá, S. Herrero, R. González-Prieto, A. Frontera and S. Chattopadhyay, *New*

J. Chem., 2017, **41**, 13585–13592; (*b*) A. Bhattacharyya, S. Sen, K. Harms and S. Chattopadhyay, *Polyhedron*, 2015, **88**, 156–163.

6 P. Bhowmik, S. Jana, P. P. Jana, K. Harms and S. Chattopadhyay, *Inorg. Chem. Commun.*, 2012, **18**, 50–56.

7 M. Das, S. Chatterjee and S. Chattopadhyay, *Inorg. Chem. Commun.*, 2011, **14**, 1337–1340.

8 S. Roy, A. Bhattacharyya, S. Purkait, A. Bauza, A. Frontera and S. Chattopadhyay, *Dalton Trans.*, 2016, **45**, 15048–15059.

9 A. Bhattacharyya, S. Roy, J. Chakraborty and S. Chattopadhyay, *Polyhedron*, 2016, **112**, 109–117.

10 S. Roy, M. G. B. Drew, A. Bauzá, A. Frontera and S. Chattopadhyay, *New J. Chem.*, 2018, **42**, 6062–6076.

11 S. Roy, M. G. B. Drew, S. Halder, P. P. Ray and S. Chattopadhyay, *New J. Chem.*, 2018, **42**, 15295–15305.

12 S. Roy, M. G. B. Drew, S. Halder, P. P. Ray and S. Chattopadhyay, *ACS Omega*, 2018, **3**, 12788–12796.

13 (*a*) N. Mahlooji, M. Behzad, H. A. Rudbari, G. Bruno and B. Ghanbari, *Inorg. Chim. Acta*, 2016, **445**, 124–128; (*b*) D. Majumdar, S. Dey, D. Das, D. K. Singh, S. Das, K. Bankura and D. Mishra, *J. Mol. Struct.*, 2019, **1185**, 112–120; (*c*) D. Majumdar, D. Das, S. Nag, M. Bhattacharyya, D. K. Singh, D. Parai, K. Bankura and D. Mishra, *J. Mol. Struct.*, 2020, **1222**, 128951; (*d*) S. Mandal, S. Roy, S. Mondal, H. A. Sparkes and S. Mohanta, *Inorg. Chim. Acta*, 2018, **482**, 612–620; (*e*) F. Zamora, H. Witkowski, E. Freisinger, J. Müller, B. Thormann, A. Albinati and B. Lippert, *J. Chem. Soc., Dalton Trans.*, 1999, 175–182.

14 K. Ghosh, K. Harms, A. Bauzá, A. Frontera and S. Chattopadhyay, *Dalton Trans.*, 2018, **47**, 331–347.

15 R.-M. Wang, Z.-F. Duan, Y.-F. He, B.-Y. Yang, Y.-P. Wang, T. Komatsu and E. Tsuchida, *J. Macromol. Sci., Part A: Pure Appl. Chem.*, 2005, **42**, 231–235.

16 M. M. Wanderley, C. Wang, C.-D. Wu and W. Lin, *J. Am. Chem. Soc.*, 2012, **134**, 9050–9053.

17 (*a*) R.-M. Wang, Z.-F. Duan, Y.-F. He and Z.-Q. Lei, *J. Mol. Catal. A: Chem.*, 2006, **260**, 280–287; (*b*) L. Ding, W. Jin, Z. Chu, L. Chen, X. Lü, G. Yuan, J. Song, D. Fan and F. Bao, *Inorg. Chem. Commun.*, 2011, **14**, 1274–1278.

18 (*a*) B. Dede, F. Karipcin and M. Cengiz, *J. Hazard. Mater.*, 2009, **163**, 1148–1156; (*b*) P. Guerriero, P. A. Vigato, D. E. Fenton and P. C. Hellier, *Acta Chem. Scand.*, 1992, **46**, 1025–1046.

19 M. Nayak, S. Sarkar, S. Hazra, H. A. Sparkes, J. A. K. Howard and S. Mohanta, *CrystEngComm*, 2011, **13**, 124–132.

20 (*a*) S. Tanase and J. Reedijk, *Coord. Chem. Rev.*, 2006, **250**, 2501–2510; (*b*) M. Kato and Y. Muto, *Coord. Chem. Rev.*, 1988, **92**, 45–83; (*c*) J.-H. Wang, P.-F. Yan, G.-M. Li, J.-W. Zhang, P. Chen, M. Suda and Y. Einaga, *Inorg. Chim. Acta*, 2010, **363**, 3706–3713.

21 S. Gambarotta, F. Arena, C. Floriani and P. F. Zanazzi, *J. Am. Chem. Soc.*, 1982, **104**, 5082–5092.

22 (*a*) P. Hobza and R. Zahradník, *Chem. Rev.*, 1988, **88**, 871–897; (*b*) K. Müller-Dethlefs and P. Hobza, *Chem. Rev.*, 2000, **100**, 143–168; (*c*) P. Hobza, R. Zahradník and K. Müller-Dethlefs, *Collect. Czech. Chem. Commun.*, 2006, **71**, 443–531; (*d*) K. E. Riley, M. Pitoňak, P. Jurečka and P. Hobza, *Chem. Rev.*, 2010, **110**, 5023–5063; (*e*) K. E. Riley and P. Hobza, *Acc. Chem. Res.*, 2013, **46**, 927–936; (*f*) A. S. Mahadevi and G. N. Sastry, *Chem. Rev.*, 2016, **116**, 2775–2825; (*g*) J. Řezáč and P. Hobza, *Chem. Rev.*, 2016, **116**, 5038–5071; (*h*) F. Biedermann and H.-J. Schneider, *Chem. Rev.*, 2016, **116**, 5216–5300.

23 J. S. Murray, P. Lane and P. Politzer, *J. Mol. Model.*, 2009, **15**, 723–729.

24 J. S. Murray, K. E. Riley, P. Politzer and T. Clark, *Aust. J. Chem.*, 2010, **63**, 1598–1607.

25 P. Politzer, J. S. Murray and T. Clark, *Phys. Chem. Chem. Phys.*, 2013, **15**, 11178–11189.

26 A. Bauzá, T. J. Mooibroek and A. Frontera, *ChemPhysChem*, 2015, **16**, 2496–2517.

27 A. Bauzá, T. J. Mooibroek and A. Frontera, *Angew. Chem., Int. Ed.*, 2013, **52**, 12317–12321.

28 (*a*) S. J. Grabowski, *Phys. Chem. Chem. Phys.*, 2014, **16**, 1824–1834; (*b*) S. Thakur, R. M. Gomila, A. Frontera and S. Chattopadhyay, *CrystEngComm*, 2021, **23**, 5087–5096.

29 R. L. Davidovich, V. Stavila, D. V. Marinin, E. I. Voit and K. H. Whitmire, *Coord. Chem. Rev.*, 2009, **253**, 1316–1352.

30 (*a*) G. Mahmoudi, A. Bauzá and A. Frontera, *Dalton Trans.*, 2016, **45**, 4965–4969; (*b*) M. S. Gargari, V. Stilinović, A. Bauzá, A. Frontera, P. McArdle, D. V. Derveer, S. W. Ng and G. Mahmoudi, *Chem. – Eur. J.*, 2015, **21**, 17951–17958.

31 C. Gourlaouen, O. Parisel and H. Gérard, *Dalton Trans.*, 2011, **40**, 11282–11288.

32 (*a*) S. Mirdya, S. Roy, S. Chatterjee, A. Bauza, A. Frontera and S. Chattopadhyay, *Cryst. Growth Des.*, 2019, **19**, 5869–5881; (*b*) G. Mahmoudi, A. Bauzá, M. Amini, E. Molins, J. T. Magued and A. Frontera, *Dalton Trans.*, 2016, **45**, 10708–10716.

33 (*a*) C. Gourlaouen, O. Parisel and H. Gerard, *Dalton Trans.*, 2011, **40**, 11282–11288; (*b*) L. Shimoni-Livny, J. P. Glusker and C. W. Bock, *Inorg. Chem.*, 1998, **37**, 1853–1867; (*c*) R. L. Davidovich, V. Stavila, D. V. Marinin, E. I. Voit and K. H. Whitmire, *Coord. Chem. Rev.*, 2009, **253**, 1316–1352; (*d*) R. M. Gomila and A. Frontera, *J. Organomet. Chem.*, 2021, 954–955.

34 A. Bauzá, T. J. Mooibroek and A. Frontera, *Chem. Rec.*, 2016, **16**, 473–487.

35 M. S. Gargari, V. Stilinović, A. Bauzá, A. Frontera, P. McArdle, D. V. Van Derveer, S. W. Ng and G. Mahmoudi, *Chem. - Eur. J.*, 2015, **21**, 17951–17958.

36 G. Mahmoudi, E. Zangrando, M. P. Mitoraj, A. V. Gurbanov, F. I. Zubkov, M. Moosavifar, I. A. Konyaeva, A. M. Kirillov and D. A. Safin, *New J. Chem.*, 2018, **42**, 4959–4971.

37 S. J. Grabowski, *Appl. Organomet. Chem.*, 2017, **31**, e3727.

38 (*a*) P. Kumar, A. Frontera and S. K. Pandey, *New J. Chem.*, 2021, **45**, 19402–19415; (*b*) G. Mahmoudi, A. Masoudiasl, M. G. Babashkina, A. Frontera, T. Doert, J. M. White, E. Zangrando, F. I. Zubkov and D. A. Safin, *Dalton Trans.*, 2020, **49**, 17547–17551.

39 D. L. Reger, T. D. Wright, C. A. Little, J. J. S. Lamba and M. D. Smith, *Inorg. Chem.*, 2001, **40**, 3810–3814.

40 H. Fleischer and D. Schollmeyer, *Inorg. Chem.*, 2004, **43**, 5529–5536.

41 A. Morsali and A. R. Mahjoub, *Helv. Chim. Acta*, 2004, **87**, 2717–2722.
42 J. Parr, *Polyhedron*, 1997, **16**, 551–566.
43 A. Hazari, L. K. Das, A. Bauza, A. Frontera and A. Ghosh, *Dalton Trans.*, 2014, **43**, 8007–8015.
44 A. Olvera, G. Shi, H. Djieutedjeu, A. Page, C. Uher, E. Kioupakis and P. F. P. Poudeu, *Inorg. Chem.*, 2015, **54**, 746–755.
45 C. A. Randall, A. S. Bhalla, T. R. Shrout and L. E. Cross, *J. Mater. Res.*, 1990, **5**, 829–834.
46 F. Cheng, J. Liang, Z. Tao and J. Chen, *Adv. Mater.*, 2011, **23**, 1695–1715.
47 L. Zhang, Y.-Y. Qin, Z.-J. Li, Q.-P. Lin, J.-K. Cheng, J. Zhang and Y.-G. Yao, *Inorg. Chem.*, 2008, **47**, 8286–8293.
48 Y. Cheng, T. J. Emge and J. G. Brennan, *Inorg. Chem.*, 1996, **35**, 342–346.
49 D. J. Majumdar, B. Tüzün, T. K. Pal, R. V. Saini, K. Bankura and D. Mishra, *Polyhedron*, 2021, **210**, 115504.
50 (*a*) D. J. Majumdar, S. Dey, A. Kumari, T. K. Pal, K. Bankura and D. Mishra, *Spectrochim. Acta, Part A*, 2021, **254**, 119612; (*b*) L. E. Orgel, Spectra of Transition-metal Complexes, *J. Chem. Phys.*, 1955, **23**, 1004–1014.
51 (*a*) G. L. Miessler and D. A. Tarr, *Inorganic Chemistry*, Pearson Education, Upper Saddle River, N. J., 3rd edn, 2004, p. 345; (*b*) D. F. Shriver and P. W. Atkins, *Inorganic Chemistry*, W. H. Freeman and Company, New York, 4th edn, 2006, p. 459; (*c*) K. L. Haas and K. J. Franz, *Chem. Rev.*, 2009, **109**, 4921–4960.
52 R. Ahlrichs, M. Bar, M. Haser, H. Horn and C. Kolmel, *Chem. Phys. Lett.*, 1989, **162**, 165–169.
53 S. Grimme, J. Antony, S. Ehrlich and H. Krieg, *J. Chem. Phys.*, 2010, **132**, 154104.
54 F. Weigend and R. Ahlrichs, *Phys. Chem. Chem. Phys.*, 2005, **7**, 3297–3305.
55 F. Weigend, *Phys. Chem. Chem. Phys.*, 2006, **8**, 1057–1065.
56 A. Bauzá and A. Frontera, *Crystals*, 2017, **7**, 191.
57 S. Yogendra, F. Hennersdorf, A. Bauza, A. Frontera, R. Fischer and J. J. Weigand, *Angew. Chem., Int. Ed.*, 2017, **56**, 7907–7911.
58 R. F. W. Bader, *Chem. Rev.*, 1991, **91**, 893–928.
59 J. Contreras-García, E. R. Johnson, S. Keinan, R. Chaudret, J.-P. Piquemal, D. N. Beratan and W. Yang, *J. Chem. Theory Comput.*, 2011, **7**, 625–632.
60 W. Humphrey, A. Dalke and K. Schulten, *J. Mol. Graphics*, 1996, **14**, 33–38.
61 A. D. Becke and K. E. Edgecombe, *J. Chem. Phys.*, 1990, **92**, 5397.
62 T. Lu and F. Chen, *J. Comput. Chem.*, 2012, **33**, 580–592.
63 G. M. Sheldrick, *SADABS, a software for empirical absorption correction, Ver.2.05*, University of Göttingen, Göttingen, Germany, 2002.
64 *SMART & SAINT Software Reference manuals Version 6.45*, Bruker Analytical X-ray Systems, Inc., Madison, WI, 2003.
65 *SHELXTL Reference Manual Ver. 6.1*, Bruker Analytical X-ray Systems, Inc., Madison, WI, 2000.
66 G. M. Sheldrick, *SHELXTL, a software for empirical absorption correction Ver.6.12*, Bruker AXS Inc., Madison, WI, 2001.
67 O. V. Dolomanov, L. J. Bourhis, R. J. Gildea, J. A. K. Howard and H. Puschmann, OLEX2, OLEX2: a complete structure solution, refinement, and analysis program, *J. Appl. Crystallogr.*, 2009, **42**, 339–341.
68 M. Dolai, T. Mistri, A. Panja and M. Ali, *Inorg. Chim. Acta*, 2013, **399**, 95–104.
69 M. Maiti, S. Thakurta, D. Sadhukhan, G. Pilet, G. M. Rosair, A. Nonat, L. J. Charbonniere and S. Mitra, *Polyhedron*, 2013, **65**, 6–15.
70 A. B. P. Lever, *Inorganic Spectroscopy*, Elsevier, New York, 2nd edn, 1984.
71 L. K. Das, M. G. B. Drew and A. Ghosh, *Inorg. Chim. Acta*, 2013, **394**, 247–254.
72 D. K. Mishra, U. K. Singha, A. Das, S. Dutta, P. Kar, A. Chakraborty, A. Sen and B. Sinha, *J. Coord. Chem.*, 2018, **71**, 2165–2182.
73 D. Sadhukhan, A. Ray, G. Rosair, L. Charbonnière and S. Mitra, *Bull. Chem. Soc. Jpn.*, 2011, **84**, 211–217.
74 M. Amirnasr, K. J. Schenk, M. Salavati, S. Dehghanpour, A. Taeb and A. Tadjarodi, *J. Coord. Chem.*, 2003, **56**, 231–243.
75 A. W. Addison, T. N. Rao, J. Reedijk, J. V. Rijn and G. C. Verschoor, *J. Chem. Soc., Dalton Trans.*, 1984, 1349–1356.
76 J. R. Thompson, D. Snider, J. E. C. Wren, S. Kroeker, V. E. Williams and D. B. Lenzoff, *Eur. J. Inorg. Chem.*, 2017, 88–98.
77 R. L. Davidovich, V. Stavila, D. V. Marinin, E. I. Voit and K. H. Whitmire, *Coord. Chem. Rev.*, 2009, **253**, 1316–1352.
78 R. J. Gillespie and R. S. Nyholm, Inorganic Stereochemistry, *Q. Rev., Chem. Soc.*, 1957, **11**, 339–380.
79 D. L. Reger, M. F. Huff, A. L. Rheingold and B. S. Haggert, *J. Am. Chem. Soc.*, 1992, **114**, 579–584.
80 J. J. McKinnon, M. A. Spackman and A. S. Mitchell, *Acta Crystallogr., Sect. B: Struct. Sci.*, 2004, **60**, 627–668.
81 P. R. Spackman, M. J. Turner, J. J. McKinnon, S. K. Wolff, D. J. Grimwood, D. Jayatilaka and M. A. Spackman, *J. Appl. Crystallogr.*, 2021, **54**, 1006–1011.
82 R. M. Gomila, A. Bauza, T. J. Mooibroek and A. Ferontera, *CrystEngComm*, 2021, **23**, 3084–3093.
83 E. Espinosa, E. Molins and C. Leocomte, *Chem. Phys. Lett.*, 1998, **285**, 170–173.
84 (*a*) A. Bauza, I. Alkorta, J. Elguero, T. J. Mooibroek and A. Frontera, *Angew. Chem., Int. Ed.*, 2020, **59**, 17482–17487; (*b*) M. Karmakar, A. Frontera, S. Chattopadhyay, T. J. Mooibroek and A. Bauza, *Int. J. Mol. Sci.*, 2020, **21**, 7091.
85 N. Sarkar, K. Harms, A. Frontera and S. Chattopadhyay, *New J. Chem.*, 2017, **41**, 8053–8065.
86 G. Mahmoudi, E. Zangrando, B. Miroslaw, A. T. Gurbanov, M. G. Babashkina, A. Frontera and D. A. Safin, *Inorg. Chim. Acta*, 2021, **519**, 120279.